ORIGINAL ARTICLE

Densification, microstructure, and nanomechanical evaluation of pulsed electric sintered zirconia-silicon nitride reinforced Ti-6Al-4 V alloy

Olakunle Anthony Ogunmefun[1] · Peter Apata Olubambi[1] · Bamidele Lawrence Bayode[1] · Ufoma Anamu[1] · Emmanuel Olorundaisi[1] · Olusoji Ayodele[1] · Bukola Babalola[1] · Sindile Mkhatshwa[1] · Peter Odetola[1] · Kibambe Ngeleshi[1]

Abstract

In this study, the influence of silicon nitride (Si_3N_4) and zirconia (ZrO_2) ceramics was examined on the titanium alloy using the pulsed electric current sintering technique to investigate the microstructural behavior, densification, and nanomechanical properties of these composites. Si_3N_4 and ZrO_2 were dispersed in Ti-6Al-4 V at a functional pressure of 50 MPa, a sintering temperature of 1200 °C, a heating rate of 100 °C/min, and a holding time of 10 min. The ternary composite samples were prepared viz, Cs1 (Ti6Al4V-**3** vol.% Si_3N_4-**15** vol.% ZrO_2), Cs2 (Ti6Al4V-**3** vol.% Si_3N_4-**10** vol.% ZrO_2), and Cs3 (Ti6Al4V-**3** vol.% Si_3N_4-**5** vol.% ZrO_2). The bulk morphology of the composites was studied using scanning electron microscopy (SEM) equipped with EDS, and the phase contents were identified with an X-ray diffractometer (XRD). The relative density results for the tri-composites showed that the Cs1 sample recorded the highest at 99.94%, producing a fully dense sintered composite. However, there was a drop in the relative density of composites Cs2 and Cs3, recording 97.73% and 97.11%, respectively, comparable to the unreinforced Ti-6Al-4 V alloy with 98.65%. The nanoindentation examination conducted for the trio-composites showed linear mechanical responses/improvement, with Vickers hardness, from 589.31 to 865.70 MPa; nano hardness, from 6.466 to 9.441 GPa, and elastic modulus, from 113.52 to 185.95 GPa.

Keywords Pulsed electric current sintering · ZrO_2 · Ti6Al4V · Si_3N_4 · Ceramics · Nanomechanical properties

1 Introduction

For applications that involve extreme temperature technology combustion engines, such as aerospace [1], materials with high melting points, high-temperature strength, and higher temperature corrosion resistance are required due to their exceptionally high-temperature characteristics, exceptional mechanical properties, high toughness, and strength. The most popular titanium alloy, commonly employed in the aerospace sector because of its excellent extreme-temperature qualities and high strength-to-weight ratio, is the Ti-6Al-4 V (Ti64) alloy. It is made up of both α-Ti and β-Ti, hence the

name "α + β alloy of titanium," and accounts for around 50% of all titanium alloy utilization. It also contains 6% of aluminum and 4% of vanadium in weight proportion. The great strength and fatigue resistance of the alloy are credited to the α-Ti, while the β-Ti also contributes to the alloy's outstanding toughness and creep resistance. In addition, these alloys have a higher working temperature range (up to 500–600 °C) than lightweight aircraft materials like magnesium alloys, fiber-polymer, and aluminum-alloy composites, allowing them to maintain their mechanical properties at higher temperatures. Although nickel alloys and heat-resistant steels were at first the favored materials in the early stages of the creation of aviation engines, they are very heavy, and titanium-based alloys can be used in their place, particularly in fan blades and discs, to significantly decrease their weight [2, 3]. Moreover, this alloy's excellent oxidation and corrosion resistance make it extremely beneficial in the maritime and biomedical industries [4, 5]. TiAl64V alloy is a remarkable alloy useful with multiplicities of engineering applications [6]. Consequent

✉ Olakunle Anthony Ogunmefun
ogunmefunolakunleanthony@yahoo.com

1 Centre for Nanoengineering and Advanced Materials, Department of Mining, Chemical and Metallurgical Engineering, University of Johannesburg, Johannesburg, South Africa

upon these exceptional qualities, titanium-based materials are in high demand not just for aerospace applications but also in the automotive and military fields. Although they have such exceptional qualities, titanium alloys have a limited range of applications due to their high price, low hardness, poor wear characteristics, high coefficient of friction, and poor surface hardness [6, 7]. Because of this, a variety of boosting procedures have been used to enhance its natural qualities. It is inappropriate for applications that call for a combination of high strength and good wear qualities due to its poor tribological behavior [8]; hence, the objectives of this study are specifically to address these key areas of deficiencies.

Due to the Ti64 alloy's poor wear resistance and low hardness, its use in medical prostheses frequently fails. Therefore, it is achievable to greatly increase the application spectrum for Ti64 alloy for substituting other metals while preserving the current attributes by altering its manufacturing procedure. A successful approach in this direction involves adding reinforcement in the form of fibers or particles to the metal matrix. Titanium matrix composites have shown to be of great choices for usage in specialized automotive parts like valves, bushings, and fuel nozzles and also in the uses for bio-implants like hip joint replacements [9]. In comparison to other common engineering materials, the stiffness of metallic matrices, hardness, wear, creep, fatigue, and specific strength properties are improved by the dispersion of reinforcement additives into the matrix components. Several material scientists have worked cooperatively to strengthen titanium alloys with metallic nitrides and ceramic particles to improve the bulk characteristics of titanium-based composites. Zirconia (ZrO_2) and silicon nitride (Si_3N_4) particles are among the best ceramic additions with suitable qualities for reinforcing titanium alloys out of all these reinforcements. High flexural modulus, outstanding creep resistance, and high hardness features are only a few of Si_3N_4's many exceptional qualities as an advanced structural ceramic. Si_3N_4 has been found to have special properties that make it an excellent ceramic material for structural uses at extremely high temperatures, such as in thermocouple tubes, liquid metal containers, and turbine steam generators. This unified ceramic material is one of the rare ones that can tolerate very high thermal shock and thermal gradients [10, 11]. Conventional Si_3N_4 ceramic, like most ceramics, has a low fracture toughness, resulting in a low damage tolerance and poor dependability, or a low Weibull modulus. According to a review of the literature, hot-pressed Si_3N_4 has fracture toughness that is between 3 and 5 MPam$^{1/2}$ [12–15], which is insufficient for the applications that are anticipated. However, it has been found that adding particulate Zirconia, (ZrO_2) as reinforcement, increases the fracture toughness of titanium-based metal matrix or ceramics. Tetragonal ZrO_2 can be used as a strengthening material component to increase the fracture toughness of Si_3N_4 to compensate for its demerits, but this can also cause the undesirable zirconium nitride (ZrN) or, zirconium oxy-nitride (ZrON) phases to form because of the widely recognized high-temperature interactions occurring during sintering at temperatures beyond 1600 °C between the ZrO2 constituent and the Si_3N_4 matrix [16, 17].

Pulsed electric current sintering, PECS, or SPS is a cutting-edge method for sintering non-oxide ceramic materials that are difficult to sinter at low temperatures over a brief period. To quickly compact particle composites to nearly their maximum intense theoretical density, a procedure called PECS/SPS combines the creation of plasma with resistive heat and pressure [18]. Unlike conventional sintering techniques like hot isostatic pressing, hot pressing, and microwave sintering, spark plasma sintering permits the complete consolidation of composite powders to nearly full theoretical densities at a shorter sintering time and lower temperature. PECS offers a fast-solidifying approach for altering the microstructural morphology and enhancing the preservation of its grain size while limiting unfavorable impacts of grain growth. The advantage of rapid processing is that it aids in obtaining the required grain size, enhancing the mechanical properties of the completed product [19]. Spark plasma sintering may therefore be highly efficient in producing high-density ceramics and metals with fine morphology/microstructure. Bulk production of composites is economical with the aforementioned advantages of pulsed electric current sintering techniques, as it is cheaper than other conventional sintering processes [20]. Much research has been conducted concerning the ceramic dispersion strengthened Ti6Al4V, and it is determined that while the relative density of alloy composites generally decreases with the addition of ceramic particles to Ti-6Al-4 V alloy, the mechanical properties of sintered alloys are unaffected by this alteration [21]. However, the fully dense composite was produced when the temperature of the sintering process increased. Falodun et al. [21, 22] recorded success in the transformation of Ti6Al4V microstructure along the grain boundary by evenly dispersing the nanoceramic TiN/TiCN in its matrix. The relative density dropped slightly from 98.6 to 97.05% when 0.5–1.0 vol.% of TiCN was included at 1000 °C; this can be attributed to the introduced grain growth and pores situated in the matrix interior. As the temperature was increased to 1100 °C for 20 min, 99.12% relative density was obtained. Also, using the PECS/SPS, Namini et al. [23] investigated the impact of TiB_2 reinforcement on titanium-based composites. A sample with a relative density of 99.6% was made almost dense by the addition of 9.6 weight percent TiB_2. Li et al. [24], Adegbenjo et al. [25], Abe et al. [26], Kgoete et al. [27], Okoro et al., and Obadele et al. [28, 29] also conducted similar research using PECS to consolidate ceramic reinforcements in a matrix of Ti6Al4V, and their results are unanimous. Creating Ti-6Al-4 V matrix composites with dispersion-strengthened Si_3N_4, and ZrO_2 ceramic reinforcement via pulsed electric current sintering, or SPS, however, has not been documented in any published literature.

The objectives of this study are to (i) examine the synthetic process of a titanium-based MMC with the incorporation of Si_3N_4/ZrO_2 ceramic particles using the PECS or SPS technique and (ii) examine the relative density, phase constituents, microstructural evolution, and nanomechanical properties of the TMC at a high temperature of 1200 °C.

2 Experimental procedure

2.1 Powder feedstock, mixing, and sintering

The commercially available powders for this study, cp-Ti6Al4V powder (99.5% purity, APS 80–88 μm), zirconia, ZrO_2 (99.9% purity, APS 40–44 μm), and silicon nitride, Si_3N_4 (99.4% purity, APS 0.35–1.2 μm) powders were supplied by Alfa Aesar, were weighed, and combined with pre-alloyed Ti-6Al-4 V powder with a regular size of ~ 30 μm. Using SEM/EDS (JEOL JSM 7900 F), the initial powders were characterized. Figure 1 depicts the morphological characterization of the as-received raw material powders. "The SEM micrograph in Fig. 1a reveals nonporous spherical particles of Ti6Al4V alloy [29], Fig. 1b displays a round (with hollow doughnut-like) morphology with numerous satellites of ZrO_2," Fig. 1c reveals hexagonal prism particles of Si_3N_4 [30]. The ternary powders were blended respectively according to their volume fraction compositions viz, Cs1 (Ti6Al4V-**3** vol.% Si_3N_4-**15** vol.% ZrO_2), Cs2 (Ti6Al4V-**3** vol.% Si_3N_4-**10** vol.% ZrO_2), and Cs3 (Ti6Al4V-**3** vol.% Si_3N_4-**5** vol.% ZrO_2) in a tubular blender and occasioned to a simultaneous rotational/translational movement for 10 h at a relative revolution per minute of 50 (rpm) to produce a homogeneous blend. For better dispersion of the ZrO_2 and Si_3N_4 reinforcement into the matrix, steel balls with an approximate radius of 4 mm (⊘ 8 mm) were added to the composites vessel, thoroughly blended at a "ball-to-powder" weight proportion of 2:5 [31]. Spark plasma sintering, otherwise termed

PECS hybrid furnace (HHPD 25-FCT Germany), was used for the consolidation. The furnace chamber was operated under a vacuumed environment, taken through 1200 °C sintering temperature at 100 °C/min sintering rate, while powder compacts were kept under an external pressure of 50 MPa, and 10 min sintering dwell time. Sintered disk-shaped composite samples with a radius of 15 mm (⊘ 30 mm) and ~ 5 mm height were formed. Before further investigation, the resulting compacts were sandblasted to get rid of any graphite contamination.

2.2 Densification studies, crystallographic, and characterization of PECSed composites

Sandblasting was followed by the grinding of Ti-6Al-4 V-wSi_3N_4-xZrO_2 composite samples with SiC sheets, starting with P120 and successively progressing through P2000 grits, to prepare them for microstructural inspection. Thereafter, ground surfaces were polished and etched with Kroll solution. The samples were later characterized to determine the microstructural and phase constitutions of the PECSed composites. From the PECSed samples, an Anton Paar DMA 5000 density meter was used to estimate the relative densities of each sample, which is based on the principle of Archimedes. The average of the six subsequent readings was used to calculate each sample's effective density, and the rule of mixture was employed to figure out its hypothetical density. Each sample's relative density was estimated by dividing its effective/bulk density by its theoretical density ratio and then by 100% [27], and the findings obtained were used to enumerate how the Si_3N_4/ZrO_2 reinforcement particles affected the composite matrix of the titanium alloy Ti64.

2.3 Nanoindentation material characteristics

On the surface of one sample, which in this experiment demonstrated the best qualities, nanoindentation measurements
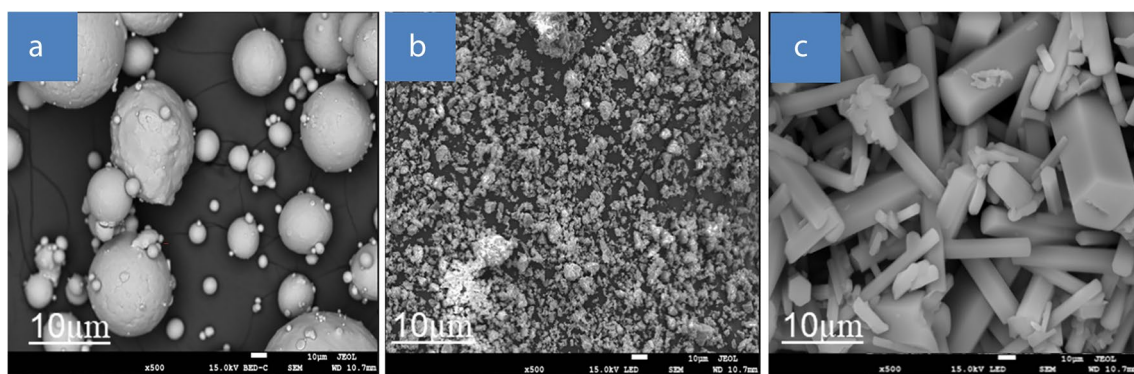
Fig. 1 SEM microstructures of as-received powder particles **a** Ti64; **b** ZrO_2, and **c** Si_3N_4

were taken. The nano-mechanical properties of the as-sintered Cs1, Cs2, and Cs3 composite specimens were evaluated using an Anton Paar Hit 300 nanoindentation tester and a Berkovich diamond indenter by ASTM E2546. The Oliver and Pharr technique calculated the nanomechanical properties from the load versus displacement curve [32]. To guarantee the validity and accuracy of the experimental results, the nanoindentation apparatus was calibrated using a fused silica reference sample. A grid of two by three points had six indentations overall for the indentation test. A distance of 3 μm exists between each indentation point. The specimen was put under a 100 mN indent peak load (Pmax). This limit was reached by rubbing on the load at a rate of 300 mN/min. The maximum load was maintained for 20 s before being removed at the same pace as it was loaded. The indentation's displacement was uninterruptedly tracked, and the indentation was recorded throughout the load-time process. The basic material characteristics derived from the nanoindentation data include Vickers indentation hardness values, nano hardness, elastic modulus, elastic strain failure, elastic recovery index, plasticity index, and yield pressure. The load–displacement curve and the Oliver and Pharr method [32] were used to find these parameters. The anticipated area of the indented imprint, Ac, is determined by the equations below, and the highest exerted force, Pmax, is used to calculate the hardness, H [32]:

The formula in Eqs. 1 and 2 illustrates the link between the max. The load applied (F_{max}) and the contact area (Ac) were utilized to calculate the nano hardness value [28, 33].

$$H = Fmax.\ Ac \tag{1}$$

$$A_c = f\left(h_c^2\right) = 24.5h_c^2 \tag{2}$$

According to Eq. 3, the calculation of the maximum "displacement depth" ($hmax$) at the "maximum applied load" ($Fmax$) combining the "displacement of the elastic surface" (he) and the "depth contact" (hc)

$$hmax = he + hc \tag{3}$$

3 Results and discussion

3.1 Characteristics of the sintered composites' microstructure

The microstructural and fundamental composition analysis using SEM/EDS of the PECSed Ti-6Al-4 V-wSi_3N_4-xZrO_2, with reinforcement additions according to the range specified by Cs1($w = 3$ vol.% Si_3N_4; $x = 15$ vol.% ZrO_2), Cs2($w = 3$ vol.% Si_3N_4; $x = 10$ vol.% ZrO_2), and

Cs3($w = 3$ vol.% Si_3N_4; $x = 5$ vol.% ZrO_2) sintered at 1200 °C, are displayed in Fig. 2. Micrographs 2 (Cs1a), (Cs2a), and (Cs3a) represent the backscattered electron images of the composites, while Fig. 2 (Cs1b), (Cs2b), and (Cs3b) depicts the EDS spectra of the three composites, showing the elemental phases of localized chemical constituents of the composite samples. The microstructures of the samples reveal that the ceramic reinforcements (Si_3N_4/ZrO_2) are evenly distributed in the matrix of the Ti-alloy matrix, with distinctive porous spots being experienced in descending patterns from Cs1 through Cs3. Also, seen from the microstructures are clearly and explicitly three distinct regions that describe the concentration of the primary/secondary phases of the corresponding composites.

According to Pennycook et al. [34], studies indicated that when an electron beam interacts with a material, it produces a visual contrast (Z-contrast) built on the differences in atomic number of the elements that exist in the substance. Furthermore, according to Chee [35, 36] in their studies, they indicated that when an electron beam interacts with a material, the contrast is built on any changes in the local electric potential due to electrically active dopant atoms. The micrographs demonstrate that the α-Ti and β-Ti phase layers came closer to one another at higher temperatures [37]. Because of the relative increase in density, higher sintering temperatures may cause enhanced grain advancement and grain boundary movement [38]. The spectrums 1, 2, and 3 in microstructure, (Fig. 2 Cs1a) with a visible characteristic of brilliant (whitish), grayish, and dark spectra suggest the presence of heavier atoms of zirconium phase, a less heavy atom titanium phase, and the lighter atom of silicon phase, respectively. When the ceramic reinforcement particles are uniformly dispersed in the matrix at the recommended temperature of 1200 °C, the resulting composite is more homogeneous and lacks porosity and cracks in its microstructure. As a result of recrystallization, an agglomeration of the silicon nitride and zirconia phases was seen in the microstructure. Krstic et al. [39] confirmed that the combination of the two ceramics exhibits outstanding mechanical properties, such as resistance to erosion by solid particles, low density, high bending strength, high elastic modulus, and fracture toughness. Put another way, because it adds to the composite's hardness qualities and eventually causes porosity to decrease, this material is incredibly strong and tough. Notably, Fig. 2 Cs2a and Cs3a micrographs show the porous spots (white arrow) in their microstructures and the nucleation of supersaturated ZrO_2 as seen (black arrow) in Cs2a, which could be a result of trapped volatiles or air bubbles during exothermic sintering process [40]. In Fig. 2 (Cs3a), porous spots are glaring in the microstructure with Si-agglomeration visibly present. The sintered necks appear to grow, and

Fig. 2 BSE micrographs and EDS spectra of the PECSed reinforced composites Cs1a, Cs2a, and Cs3a; and Cs1b, Cs2b, and Cs3c at sintering temperature of 1200 °C
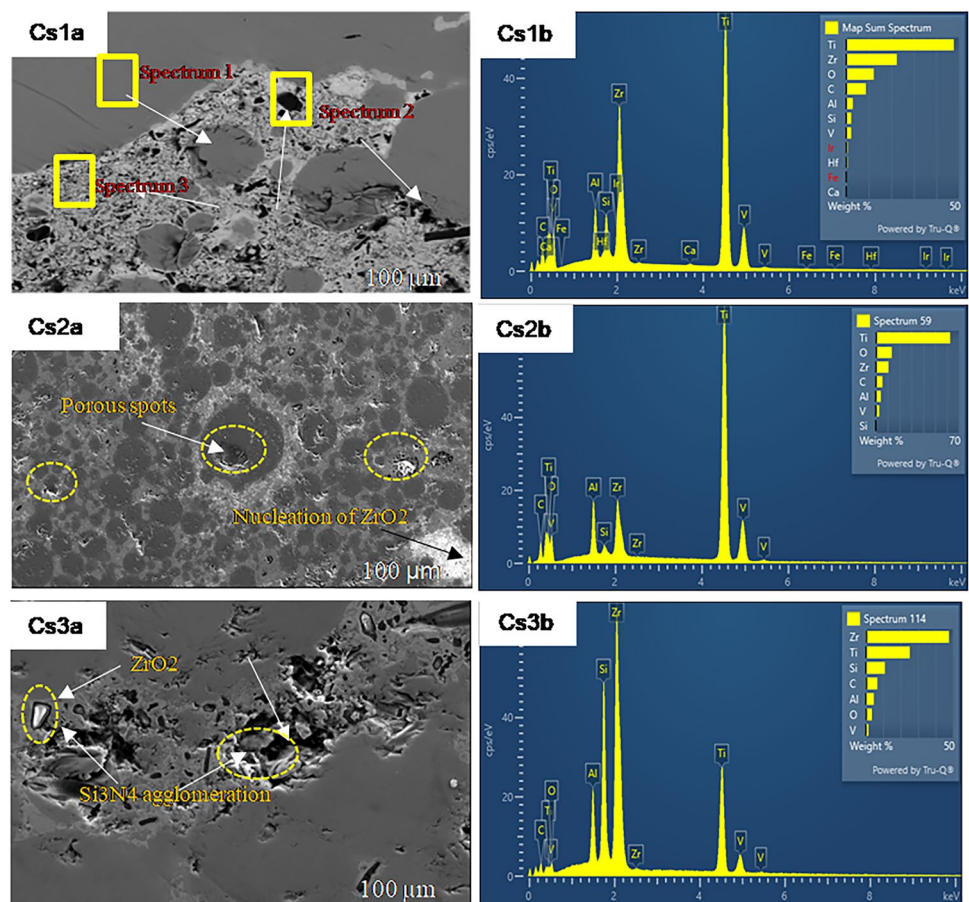
the densification zone expands further, making the grains appear coarser in the composite specimens with more porosity.

The EDS elemental layers in Fig. 3a, b, and c reveal the emerging phases in the microstructures of the PECSed composites Cs1, Cs2, and Cs3 composites at 1200 °C sintering temperature.

As depicted in the mappings, the distribution of elements, viz. Ti, Zr, Al, V, Si, and O are represented by mappings, showing the ceramic reinforcement dispersion in the matrix compositions within respective microstructures.

3.2 XRD analysis

The composition of as-sintered Ti-6Al-4 V ceramic-based samples was investigated by their corresponding XRD patterns. The results of phase analysis are presented in Fig. 4. The characteristic peaks conforming to α-Ti and β-Ti phases were indefinite in the designs of the composites with the addition of ZrO_2/Si_3N_4 ceramic particles; a decrease in the titanium's distinctive reflection is seen, nevertheless. The X-ray absorption effect can be attributed to the drop in the

intensity peak [41]. As shown on all the diffractograms, the primary phases of Ti6Al4V, ZrO_2, and Si_3N_4, and the secondary/in situ phases, viz Zr_2, Ti_2N, and SiO_2 were detected. Also, in the diffractograms, molten SiO_2 evolution in the reaction of the sintering process can be said to promote the densification of Ti6Al4V-based ceramic through the filling of the voids between particles via the liquid phase sintering mechanism. Falodun et al. [42], in one of their numerous studies on dispersion-strengthened Ti-alloy through the deployment of PECS, reported on the formation of Ti_2N intermetallic phase during sintering, with a subsequent enhancement in the mechanical properties of the consolidated composites. These results may imply that the enhancement of the mechanical characteristics of titanium-based composites is dependent on the production of intermetallic phases, as suggested by the peak intensities of the diffractogram used in this study. Figure 4 demonstrates that there was no broadening of the peaks, implying that there was no impending reaction at the start of the sintering process. The expansion of the peaks can be ascribed to ultra-fine grain particles of the starting powders and a likelihood of internal strain in the powder [43]. The peaks of several phases were seen, and
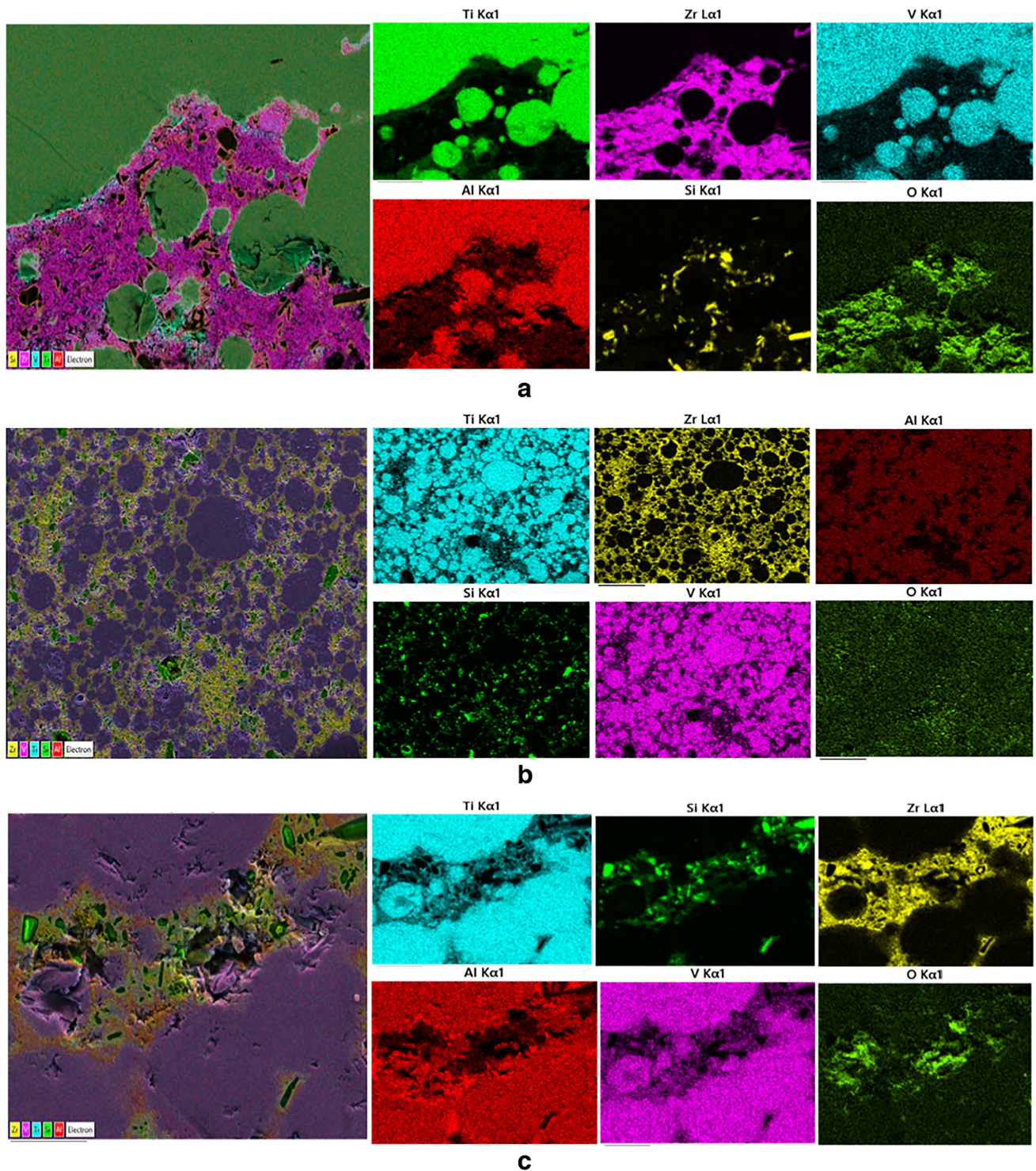
Fig. 3 EDS elemental mapping of composite **a** Cs1, **b** Cs2, and **c** Cs3 sintered at a temperature of 1200 °C

the admixed composites' interfacial phases were exposed at the appropriate temperatures. The Al and V did not exhibit any significant peak intensity. The concentrations of these phases were likely too small for X-ray to detect, making it impossible for XRD to show them.

Interestingly, the titanium nitride (Ti_2N) phase stages the highest peak intensity for all the composite samples at the same 2-θ angle of 41.566°. This predominantly could be a result of the strong affinity/reactivity of silicon nitride and Ti-alloy following Si_3N_4's instability in the titanium
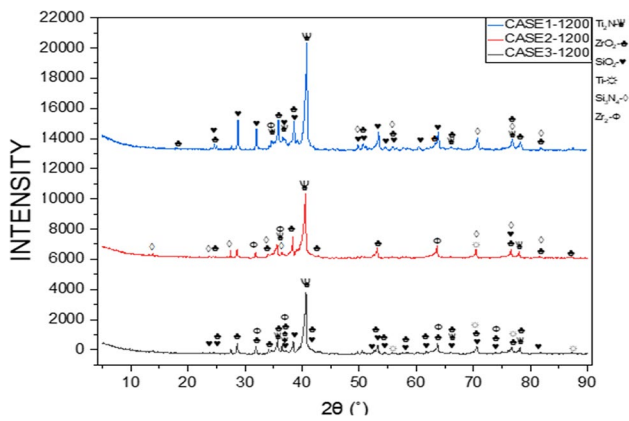
Fig. 4 XRD patterns: titanium matrix composite sintered at 1200 °C

matrix at high temperatures. In contrast to composites Cs2/Cs3, which had equal vol.% Si_3N_4, and **10** vol.% / **5** vol.% ZrO_2, respectively, the addition of equal vol.% Si_3N_4 and **15** vol.% ZrO_2 of composite Cs1 demonstrated that the intensity of the diffraction peaks was increased and broadened, with a series of peak overlaps of phases consisting of Ti, Si_3N_4, SiO_2, Ti_2N, and ZrO_2. It is significant to highlight that the intermetallic/refractory nature of the in situ or secondary phases will enhance the characteristics of the composite materials produced.

3.3 Density and porosity calculations for composites sintered at 1200 °C

The numerical values and response bar chart of the experimentally measured relative density and porosity are represented in Fig. 4. On the relative density of the TMC, Fig. 4 displays the effects of a uniform volume fraction of Si_3N_4 and a variable volume % of ZrO_2 on titanium alloy, Ti6Al4V at an operating temperature of 1200 °C, and 10 min holding time. The relative density recorded as shown in Table 1 suggests composite sample Cs1, (Ti6Al4V-**3** vol.% Si_3N_4-**15**

Table 1 Sintering conditions and relative density of Ti6Al4V-wSi_3N_4-$xZrO_2$ at 1200 °C

Sintering materials	Temp. (°C)	Time (Min)	Pressure (MPa)	Relative density (%)
Unreinforced TI-6Al-4 V	1200	10	50	98.65
Ti6Al4V-3Si$_3$N$_4$-15% ZrO$_2$	1200	10	50	99.94
Ti6Al4V-3Si$_3$N$_4$-10% ZrO$_2$	1200	10	50	97.73
Ti6Al4V- 3Si$_3$N$_4$-5% ZrO$_2$	1200	10	50	97.11

vol.% ZrO_2) increased significantly to practically reach full densification, whereas composite samples, Cs2 and Cs3, slightly decreased in densification, comparative of the unreinforced matrix sample.

Table 1 is the tabulation for sintering parameters and the relative density of the unreinforced matrix and reinforced composites, while Fig. 5 is the response bar illustrating the relative densification of the sample constituents/composites. As seen from the table, the density drop in Cs2 and Cs3 could be explained by increased porosity, a higher sintering temperature, and a longer introduction time for reinforcement, which results in a lower material density [44, 45]. This provides a clear indication that the addition of variable volume percentages, 5–15 vol.% of ZrO_2 has a significant impact during the PECS process. This phenomenon may be connected to the beginning of grain growth and the organization of internal pores in the structures. The reduction in the porosity level upon the addition of the ceramics could be connected to the sintering temperature adopted in this study as confirmed [22], which increases the material's density. Teber et al. [44] also confirm that a lower porosity level for composites is indicative of a higher relative density, which increases their material efficiency to improve their mechanical performance.

3.4 Mechanical quantities of sintered composites

The elastic modulus (EIT) and hardness (H) of the ternary composite Ti6Al4V-wSi_3N_4-$xZrO_2$ of the sintered composites Cs1, Cs2, and Cs3 made by nanoindentation are shown in Table 2 and Fig. 6. Notably, the elastic modulus values exhibit the same pattern as Vickers hardness and the nano hardness. All composite samples' hardness and elastic modulus values are improved, as seen, by the introduction of ceramics. Understandably, the ceramic reinforcement reduces the energy at the grain boundary
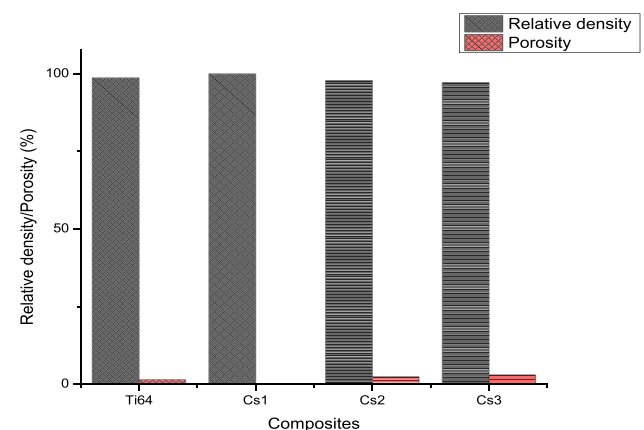

Fig. 5 Relative density and porosity of sintered Ti64-wSi_3N_4-$xZrO_2$ composites at 1200 °C

Table 2 Nanoindentation of PECSed Ti64-wZrO$_2$-xSi$_3$N$_4$, including elastic modulus, reduced elastic modulus, Vickers indentation hardness (HVIT), and nano hardness (HIT) of composites, Cs1, Cs2, and Cs3 at 1200 °C sintering temperature

Samples	Elastic modulus, (EIT) (GPa)	Reduced E modulus (E_r) (GPa)	Vickers hardness (HVIT) (MPa)	Nano hardness (HIT) (MPa)	Maximum depth (nm)
Cs1	185.95	175.92	865.70	9441.4	141.76
Cs2	151.61	134.73	670.11	7519.2	175.22
Cs3	127.64	118.67	657.27	6935.1	178.13
Ti6Al4V	113.52	101.13	589.31	6465.7	188.10

Fig. 6 Relationship graph of elastic modulus with Vickers indentation hardness and nano hardness for sintered composites Cs1, Cs2, and Cs3 at 1200 °C
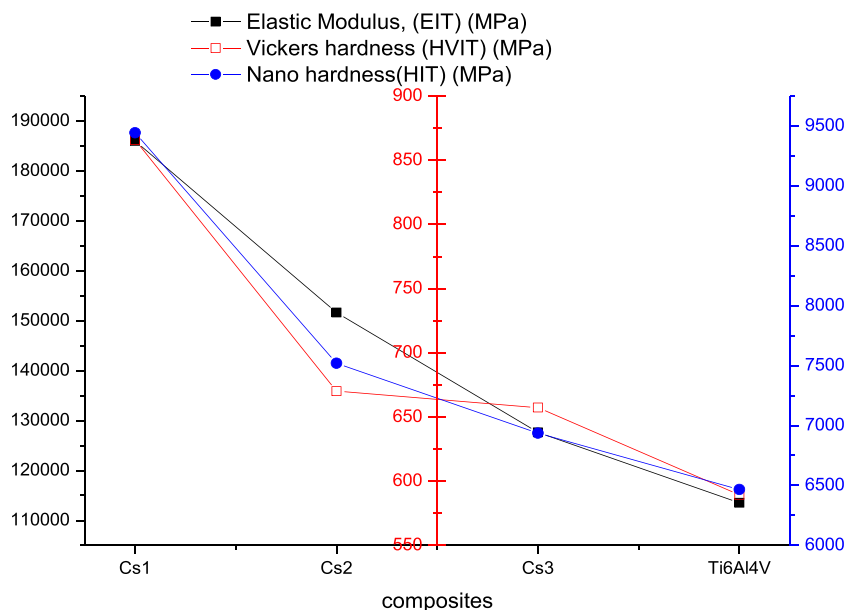
and weakens movability, further preventing dislocation movement. This barrier prevents the grains from growing too much at a high temperature, which keeps them stable and makes them harder [46, 47]. From this study, Vickers hardness improved from 589.31 to 865.70 MPa, nano hardness from 6.466 to 9.441 GPa, and elastic modulus enhanced from 113.52 to 185.95 GPa. The enhancement of Ti6Al4V matrix composites in terms of hardness and elastic moduli may be attributed to the composite's lower β-phase content. Previous studies have shown that the orthorhombic α-phase typically has higher hardness and elastic modulus than the β-phase with BCC crystalline structure [48, 49]. As a result, hardness and elastic modulus are decreased by a high β-phase concentration. These findings also suggest that adding reinforcement particles to Ti6Al4V particles improves the alloy's nanomechanical characteristics by limiting free dislocation movement in the composites. A substance's strength is inversely correlated with its hardness, meaning that harder materials have more strength [50].

The Si$_3$N$_4$-ZrO$_2$ reinforcements are therefore thought to have acted as stabilizers, boosting the percentage of a

martensitic phase in the Ti6Al4V composite. As such, composite Cs1 exhibits a proportionally highest value of both quantities (hardness and elastic modulus values), followed by Cs2, and composite Cs3. In the case of composite, Cs1, the comparatively high volume fractions of the ceramic reinforcements in the titanium matrix composite at elevated temperature [51, 52] are said to be responsible for increasingly high hardness values, and it is as relative to its density percentage [44]. Literature also suggests that the size, composition, reduced porosity, grain refinement, and dispersion hardening effect brought on by the titanium matrix reinforcing phases are some of the factors that could be responsible for the improvement in hardness [53].

3.5 Sintered titanium matrix composites' nanoindentation studies

The load–displacement curves for the Cs1, Cs2, and Cs3 dispersed strengthened titanium matrix composites appear to show the average values of six indentations. Figure 7's representation of the hardness-penetration depth graphs accurately depicts the three distinct zones, linear profiles,
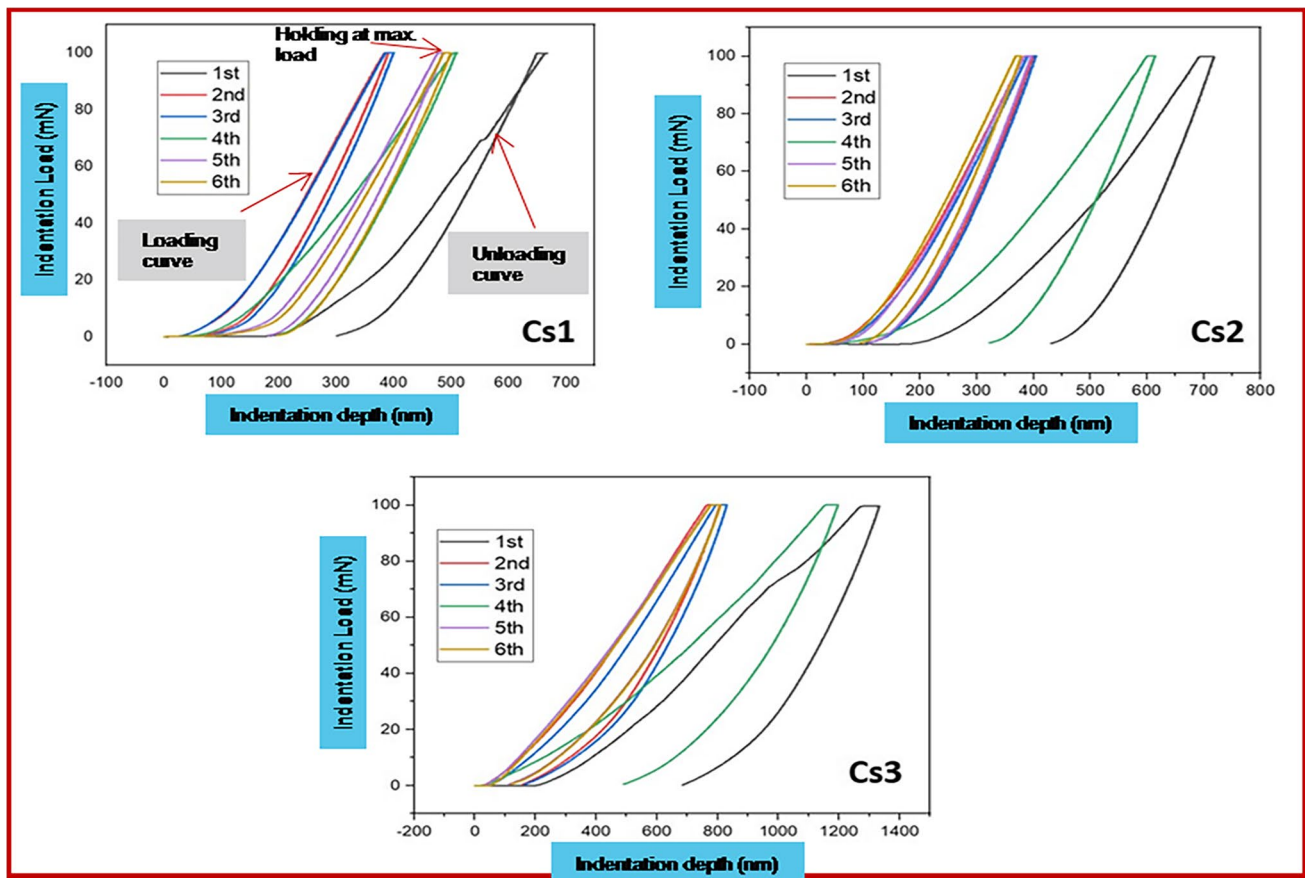
Fig. 7 The changes of applied load vs. penetration depth in the indentation test for Cs1-(Ti64-3Si$_3$N$_4$-15ZrO$_2$), Cs2-(Ti64-3Si$_3$N$_4$-10ZrO$_2$), and Cs3-(Ti64-3Si$_3$N$_4$-5ZrO$_2$) at sintering temperature of 1200 °C

and varying hardness that are visible. The composites that had been PECSed showed consecutive loading and unloading behaviors because of the applied load, as indicated by the indentation curves. Although the dispersed reinforcing particles were present, they caused a difference in the elastic–plastic deformation behavior. Without a doubt, unreinforced Ti6Al4V has the greatest penetration depth [21, 28, 54, 55], followed by Cs3, Ti6Al4V-3 vol.% Si$_3$N$_4$-15 vol.% ZrO$_2$; Cs2, Ti6Al4V-3 vol.% Si$_3$N$_4$-15 vol.% ZrO$_2$; and Cs1, Ti6Al4V-3 vol.% Si$_3$N$_4$-15 vol.% ZrO$_2$. It appears that increasing the ceramic content (Si$_3$N$_4$/ZrO$_2$) enhanced the titanium matrix composites' resistance to plastic deformation under indentation. This suggests an increase in hardness and stiffness as a result of load transfer from the matrix to the reinforcement [28]. This suggests that the reinforced Ti6Al4V alloys have higher plastic deformation resistance. The BCC strengthening phase and lattice distortion created by the reinforcement particles are also responsible for the strengthening mechanism displayed by the reinforced Ti6Al4V alloys. In a recent investigation, Li et al. [56] reported making a comparable observation. In addition, the resulting BCC phase reduces sliding planes,

prevents interplanar dislocations, thwarts plastic deformation, and stabilizes microstructure [57]. With a maximum indentation depth of 188.10 nm, the Ti6Al4V alloy showed substantial plastic deformation. When reinforcements were added, penetration shrank from 178.13 to 141.76 nm. With the inclusion of the appropriate reinforcements, however, the lower penetration depth suggests plastic deformability [58]. Ti-6Al-4 V-3 vol.% Si$_3$N$_4$-15 vol.% ZrO$_2$ had the best resistance to indentation loads concerning penetration depth. This research is in line with the work of Asl et al. [59]. These findings demonstrate that increasing the volume fractions of zirconia additives in the composites promotes an increasing resistance to plastic deformation during indentation. Several reasons can be alluded to a decrease in hardness and elastic modulus, as seen in Cs2 and Cs3, but they are not limited to matrix-reinforcement particles' poor interfacial bonding [60]. However, the higher elastic modulus shown in Cs1 by the PECSed composite suggests a proportionate increase in stiffness, and it can also be attributed to the development of in situ exothermic reaction during the sintering process (secondary phases); a decrease in crystallite size and an increase in lattice strain brought on by the inclusion of refractory

particles are contributory to the mechanical characteristics being strengthened [60].

4 Conclusion

A study was conducted on varied ceramic additions to the matrix of titanium alloy, Ti6Al4V alloy powder, to form composites Cs1, Cs2, and Cs3 ternary-composites which were consolidated with a pulsed electric current sintering furnace at a temperature of 1200 °C, with an external pressure of 50 MPa, for 10 min holding time, and a sintering rate of 100 °C/min.

From the investigation, the following deductions were made, viz.:

- Pulsed electric current sintering technique successfully achieved the consolidation of ternary composites Ti6Al4V-wSi_3N_4-$xZrO_2$ for all composite samples, and process conditions, such as temperature, pressure, and duration were found to have influenced the final composite properties via the relative density recorded.
- The chosen refractory reinforcement (Si_3N_4-ZrO_2), with volume fraction (3% vol. Si_3N_4), and varied (5–15% vol. ZrO_2) produced TMC with near-full densification and best nanomechanical properties at 1200 °C sintering temperature.
- The pulsed electric sintered composites of samples Cs1 (Ti-6Al-4 V-3 vol.% Si_3N_4-15 vol.% ZrO_2) produced composites of almost a non-porous microstructure of uniformly dispersed ceramic reinforcement in the titanium alloy matrix, attaining practically full theoretical relative density with composite Cs1 at 99.94%, comparable to the unreinforced Ti6Al4V alloy at 98.65%.
- It was observed that a reduction of ZrO_2 reinforcing ceramic particles (from 15 to 10 to 5 vol.%) in composites Cs1, Cs2, and Cs3, respectively, affected the composites. As Cs1 improved in relative density and mechanical properties, Cs2 and Cs3 dropped.
- The trio-composites, Cs1 (Ti-6Al-4 V-3 vol.% Si_3N_4-15 vol.% ZrO_2), Cs2 (Ti-6Al-4 V-3 vol.% Si_3N_4-10 vol.% ZrO_2), and Cs3 (Ti-6Al-4 V-3 vol.% Si_3N_4–5 vol.% ZrO_2) emerged non-destructive in situ phases of Ti_2N and SiO_2 during sintering at 1200 °C. These various interdiffusion reactions of both primary and in situ phases assisted further densification of the composites, enhancing the mechanical properties of the fabricated composites.
- From this study, Vickers hardness improved from 589.31 to 865.70 MPa, nano hardness from 6.466 to 9.441 GPa, and elastic modulus enhanced from 113.52 to 185.95 GPa. The enhancement of Ti6Al4V matrix composites in terms of hardness and elastic moduli may be attributed to the composite's lower β-phase content.

5 Recommendation

This noble study calls for in-depth research for a possible upgrade of the ternary composition of elemental powders used in this research via pulsed electric current sintering technique, a careful formulation of workable design parameters to achieve complete densification of feedstock, and by extension, achieving an excellent product with the best mechanical properties for high-temperature applications, such as in the aerospace, nuclear, military, and turbine engines.

Author contribution OAO: management and coordination of responsibility for the research activity planning and execution. POlubambi: supervision and verification of facts about the review, whether as a part of the activity or separate, of the reproducibility of results and other research outputs. LB: preparation, creation, and/or presentation of the published work by those from the original research group, specifically critical review, commentary, or revision—including pre- or post-publication stages. SA: oversight and leadership responsibility for the research activity planning and execution, including mentorship external to the core team. EO: literature reviews. OA: preparation, creation, and/or presentation of the published work by those from the original research group, specifically critical review, commentary, or revision—including pre- or post-publication stages. BB: preparation, creation, and/or presentation of the published work by those from the original research group, specifically critical review, commentary, or revision—including pre- or post-publication stages. SM: microscopy. POdetola: literature reviews. KN: laboratory analysis and data management.

Data availability Data will be made available on request.

Declarations

Ethical approval Not applicable.

Consent to participate Yes.

Consent for publication Yes.

Competing interests The authors declare no competing interests.

References

1. Bakshi SR et al (2011) Spark plasma sintered tantalum carbide: effect of pressure and nano-boron carbide addition on microstructure and mechanical properties. Mater Sci Eng: A 528(3):1287–1295

2. Zhu Y et al (2012) Effect of processing parameters on the hot deformation behavior of as-cast TC21 titanium alloy. Mater Des 33:264–272

3. Abe JO, Popoola API, Popoola OM (2019). Influence of varied process parameters on the microstructure, densification and microhardness of spark plasma sintered Ti-6Al-4V/h-BN binary composite. In: IOP Conference Series: Materials Science and Engineering (vol 689, no. 1). IOP Publishing, p 012005

4. Peters M, Leyens C (eds) (2003) Titanium and titanium alloys: fundamentals and applications. Wiley

5. Geetha M et al (2009) Ti-based biomaterials, the ultimate choice for orthopaedic implants–a review. Prog Mater Sci 54(3):397–425

6. Lisiecki A, Piwnik J (2016) Tribological characteristic of titanium alloy surface layers produced by diode laser gas nitriding. Arch Metall Mater 61(2A):543–552

7. Ezugwu E, Bonney J, Yamane Y (2003) An overview of the machinability of aeroengine alloys. J Mater Process Technol 134(2):233–253

8. Attabi S et al (2019) Electrochemical and tribological behavior of surface-treated titanium alloy Ti–6Al–4V. J Bio-and Tribo-Corrosion 5:1–11

9. Moghadasi K et al (2022) A review on biomedical implant materials and the effect of friction stir based techniques on their mechanical and tribological properties. J Mater Res Technol 17:1054–1121

10. Hoffmann MJ (2001) Si_3N_4 ceramics, structure and properties of. Encyclopedia of Materials: Science and Technology, pp 8469–8471

11. Drouet C et al (2017) Types of ceramics: material class. Advances in Ceramic Biomaterials. Elsevier, pp 21–82

12. Zhao W, Cui J, Rao P (2018) Effect of molten zone ablated by femtosecond lasers on fracture toughness of Si3N4 measured by SEVNB method. J Eur Ceram Soc 38(4):2243–2246

13. Sayyadi-Shahraki A et al (2019) Densification and mechanical properties of spark plasma sintered Si3N4/ZrO2 nano-composites. J Alloy Compd 776:798–806

14. Haubner R et al (2003) High performance non-oxide ceramics II, vol 102. Springer

15. Ogunmefun OA et al (2023) A critical review of dispersion strengthened titanium alloy fabricated through spark plasma sintering techniques. J Alloys Compd 960:170407

16. Lange FF (1980) Compressive surface stresses developed in ceramics by an oxidation-induced phase change. J Am Ceram Soc 63(1–2):38–40

17. Lange F, Falk L, Davis B (1987) Structural ceramics based on Si3N4–ZrO2 (+ Y2O3) compositions. J Mater Res 2(1):66–76

18. Falodun OE et al (2018) Influence of spark plasma sintering on microstructure and wear behaviour of Ti-6Al-4V reinforced with nanosized TiN. Trans Nonferrous Metals Soc China 28(1):47–54

19. Feng H et al (2005) Rapid synthesis of Ti alloy with B addition by spark plasma sintering. Mater Sci Eng: A 390(1–2):344–349

20. Dudina DV, Georgarakis K, Olevsky EA (2023) Progress in aluminium and magnesium matrix composites obtained by spark plasma, microwave, and induction sintering. Int Mater Rev 68(2):225–246

21. Falodun OE et al (2023) The effect of TiN-TiB2 on the microstructure, wear, and nanoindentation behavior of Ti6Al4V-Ni-Cr matrix composites. J Mater Eng Perform 32(12):5566–5575

22. Falodun OE et al (2020) Effect of TiN and TiCN additions on spark plasma sintered Ti–6Al–4V. Part Sci Technol 38(2):156–165

23. Namini AS, Azadbeh M, Asl MS (2017) Effect of TiB2 content on the characteristics of spark plasma sintered Ti–TiBw composites. Adv Powder Technol 28(6):1564–1572

24. Li A et al (2018) Microstructure and mechanical properties of Y2O3 reinforced Ti6Al4V composites fabricated by spark plasma sintering. J Alloy Compd 768:49–56

25. Adegbenjo AO, Obadele BA, Olubambi PA (2018) Densification, hardness and tribological characteristics of MWCNTs reinforced Ti6Al4V compacts consolidated by spark plasma sintering. J Alloy Compd 749:818–833

26. Abe J, Popoola A, Popoola O (2020) Consolidation of Ti6Al4V alloy and refractory nitride nanoparticles by spark plasma sintering method: microstructure, mechanical, corrosion and oxidation characteristics. Mater Sci Eng: A 774:138920

27. Kgoete F et al (2018) Influence of Si3N4 on Ti-6Al-4V via spark plasma sintering: microstructure, corrosion and thermal stability. J Alloy Compd 763:322–328

28. Okoro AM et al (2019) Nanoindentation studies of the mechanical behaviours of spark plasma sintered multiwall carbon nanotubes reinforced Ti6Al4V nanocomposites. Mater Sci Eng: A 765:138320

29. Obadele BA et al (2015) Improving the tribocorrosion resistance of Ti6Al4V surface by laser surface cladding with TiNiZrO2 composite coating. Appl Surf Sci 345:99–108

30. Rakotoniaina JP et al (2005) Distribution and formation of silicon carbide and silicon nitride precipitates in block-cast multicrystalline silicon. In: Proceedings of the 20th European Photovoltaic Solar Energy Conference and Exhibition, Barcelona, Spain

31. Ujah C et al (2019) Optimisation of spark plasma sintering parameters of Al-CNTs-Nb nano-composite using Taguchi design of experiment. Int J Adv Manuf Technol 100(5):1563–1573

32. Oliver WC, Pharr GM (2004) Measurement of hardness and elastic modulus by instrumented indentation: advances in understanding and refinements to methodology. J Mater Res 19(1):3–20

33. Hynowska A et al (2012) Nanostructured β-phase Ti–31.0 Fe–9.0 Sn and sub-μm structured Ti–39.3 Nb–13.3 Zr–10.7 Ta alloys for biomedical applications: microstructure benefits on the mechanical and corrosion performances. Mater Sci Eng: C 32(8):2418–2425

34. Pennycook S, Rafferty B, Nellist P (2000) Z-contrast imaging in an aberration-corrected scanning transmission electron microscope. Microsc Microanal 6(4):343–352

35. Chee AK (2020) Unravelling new principles of site-selective doping contrast in the dual-beam focused ion beam/scanning electron microscope. Ultramicroscopy 213:112947

36. Chee AK (2016) Quantitative dopant profiling by energy filtering in the scanning electron microscope. IEEE Trans Device Mater Reliab 16(2):138–148

37. Maseko S, Popoola A, Fayomi O (2018) Characterization of ceramic reinforced titanium matrix composites fabricated by spark plasma sintering for anti-ballistic applications. Def Technol 14(5):408–411

38. Miklaszewski A, Garbiec D, Niespodziana K (2018) Sintering behavior and microstructure evolution in cp-titanium processed by spark plasma sintering. Adv Powder Technol 29(1):50–57

39. Krstic Z, Krstic VD (2012) Silicon nitride: the engineering material of the future. J Mater Sci 47:535–552

40. Hooshmand S, Nordin J, Akhtar F (2019) Porous alumina ceramics by gel casting: effect of type of sacrificial template on the properties. Int J Ceram Eng Sci 1(2):77–84

41. Kenel C et al (2017) In situ investigation of phase transformations in Ti-6Al-4V under additive manufacturing conditions combining laser melting and high-speed micro-X-ray diffraction. Sci Rep 7(1):16358

42. Falodun OE et al (2018) Effect of sintering parameters on densification and microstructural evolution of nano-sized titanium nitride reinforced titanium alloys. J Alloy Compd 736:202–210

43. Sritharan T, Boey F, Srinivas A (2007) Synthesis of complex ceramics by mechanochemical activation. J Mater Process Technol 192:255–258

44. Teber A et al (2012) Effect of SPS process sintering on the microstructure and mechanical properties of nanocrystalline TiC for tools application. Int J Refract Metal Hard Mater 30(1):64–70

45. Kgoete F, Popoola A, Fayomi O (2018) Influence of spark plasma sintering on microstructure and corrosion behaviour of Ti-6Al-4V alloy reinforced with micron-sized Si3N4 powder. Def Technol 14(5):403–407

46. Stalin B et al (2021) Effect of titanium diboride ceramic particles on mechanical and wear behavior of Cu-10 wt% W alloy composites processed by P/M route. Vacuum 184:109895

47. Ďurišin J et al (2004) Effect of the MgO particles on the nanocrystalline copper grain stability. Mater Lett 58(29):3796–3801

48. Faria ACL et al (2011) Wear resistance of experimental titanium alloys for dental applications. J Mech Behav Biomed Mater 4(8):1873–1879

49. Ehtemam-Haghighi S et al (2016) Influence of Nb on the et al″martensitic phase transformation and properties of the newly designed Ti–Fe–Nb alloys. Mater Sci Eng: C 60:503–510

50. Zhang P, Li S, Zhang Z (2011) General relationship between strength and hardness. Mater Sci Eng: A 529:62–73

51. Cheng J et al (2018) Microstructure, mechanical and tribological properties of TiAl-based composites reinforced with high volume fraction of nearly network Ti2AlC particulates. J Mater Sci Technol 34(4):670–678

52. Wang LF et al (2015) Microstructure and mechanical properties of TiB-Ti/Ti-6Al-4V composites fabricated by spark plasma sintering. Appl Mech Mater 782:107–112

53. Namini AS et al (2019) Effect of TiB2 addition on the elevated temperature tribological behavior of spark plasma sintered Ti matrix composite. Compos Part B: Eng 172:271–280

54. Abe JO, Popoola OM, Popoola AP (2023) Assessment of nanomechanical and tribological performance of refractory nitride-reinforced titanium alloy matrix composites developed by spark plasma sintering. JOM 75(3):791–805

55. Cai C et al (2019) In-situ preparation and formation of TiB/Ti-6Al-4V nanocomposite via laser additive manufacturing: microstructure evolution and tribological behavior. Powder Technol 342:73–84

56. Tian Y et al (2022) Tribological property and subsurface damage of nanotwinned Cu/FeCoCrNi high entropy alloy nanolaminates at various scratching velocities and normal loads. Tribol Int 169:107435

57. Mekgwe GN et al (2021) Fabrication of graphite reinforced TiCxNy by spark plasma sintering technique: a comparative assessment of microstructural integrity and nanoindentation properties. Vacuum 187:110144

58. Akinwamide SO, Akinribide OJ, Olubambi PA (2021) Microstructural evolution, mechanical and nanoindentation studies of stir cast binary and ternary aluminium based composites. J Alloy Compd 850:156586

59. Asl MS et al (2020) Nanoindentational and conventional mechanical properties of spark plasma sintered Ti–Mo alloys. J Market Res 9(5):10647–10658

60. Jarząbek DM (2018) The impact of weak interfacial bonding strength on mechanical properties of metal matrix–ceramic reinforced composites. Compos Struct 201:352–362